Theory and simulation of short intense laser pulse propagation in capillary tubes with wall ablation

M. Veysman
Laboratoire de Physique des Gaz et des Plasmas, CNRS-Université Paris Sud 11, 91405 Orsay, France and Institute for High Energy Densities, Moscow, Russia

B. Cros
Laboratoire de Physique des Gaz et des Plasmas, CNRS-Université Paris Sud 11, 91405 Orsay, France

N. E. Andreev
Institute for High Energy Densities, Moscow, Russia

G. Maynard
Laboratoire de Physique des Gaz et des Plasmas, CNRS-Université Paris Sud 11, 91405 Orsay, France

(Received 29 November 2005; accepted 10 April 2006; published online 24 May 2006)

The theory and simulations of short intense laser pulses propagating in capillary tubes, whose properties are changed in time and space under the action of the laser field, are presented. A hybrid approach has been used in which the dynamics of fields inside the capillary tube is described analytically, whereas the ionization, heating, and expansion of the plasma created at the inner wall of the tube under the action of the transverse energy flux are calculated by numerical simulation. This hybrid method has allowed to determine the behavior of high laser fluxes guided over large distances. The threshold value for the incident intensity at which plasma creation plays a significant role has been estimated analytically and confirmed by numerical results. For intensities above the threshold, the transmission becomes highly sensitive to the energy of the laser pulse, being minimum at the intensity level for which the electron temperature of the capillary wall slightly exceeds the Fermi level and the electron collision frequency has a maximum. © *2006 American Institute of Physics*. [DOI: 10.1063/1.2201060]

I. INTRODUCTION

Several applications of ultraintense, short laser pulses, such as laser plasma accelerators,[1] harmonic generation,[2,3] and x-ray lasers[4,5] require the achievement of high laser intensity over distances much longer than the Rayleigh length. The use of a capillary tube as a waveguide with inner radius of the order of the laser pulse waist has been shown[6–12] to meet this requirement. The laser pulse propagation inside a capillary tube in the absence of wall heating and ablation has been studied extensively.[6,7,9,11]

For moderate laser pulse intensities a theory of the nonlinear laser pulse propagation in metallic waveguides was developed under conditions where the temperature of capillary walls heated by the laser pulse does not exceed the Fermi temperature, and the processes of ionization and expansion of the capillary wall, as well as modifications of the real part of the permittivity and gradients of permittivity of the plasma, created at the wall, can be neglected.[10]

The model presented in this paper is aimed at the self-consistent description of high intensity laser pulse propagation in a capillary tube, taking full account of ionization, heating, and expansion of the capillary walls. These processes should be considered for the description of the propagation of ultraintense laser pulses (with peak intensity $I_L \sim 10^{16}-10^{20}$ W/cm^2) through thin (inner radius, R_0, of the order of tens of μm) capillary tubes, for which the transverse energy flux into the capillary tube wall, $S_r(R_0)$, is substantial, $S_r(R_0) > 10^{12}$ W/cm^2, and leads to a significant modification of the wall properties. It is shown that the modification of the wall properties can lead to a significant (up to an order of magnitude) increase of laser energy losses inside the capillary walls. The characteristics of the resulting plasma, which will expand inside the tube, is of great importance for planned experiments on x-ray generation in capillaries for which this plasma is expected to serve as an active medium.

In Sec. II, the equations describing the propagation of circularly polarized laser fields inside the capillary tube are derived. An analytical solution is proposed for the fields inside the tube. This approach allows to study the influence of the capillary walls dynamics on the structure of the electromagnetic field and the properties of the plasma created inside the capillary tube.

A hybrid numerical code has been constructed in which the fields inside the tube are calculated by the analytical solution of Sec. II, whereas the evolution of the plasma created at the inner surface of the wall is determined by solving numerically a system of hydrodynamic equations[13] using the calculated value of the density of the inverse bremsstrahlung absorption rate. The hydrodynamic equations used to describe plasma dynamics are presented in Sec. III.

For many practical applications the fields inside the tube have a simple structure quickly evaluated through the formula of Sec. II. Therefore our hybrid method leads to fast numerical calculations, allowing to analyze the guiding of high intensity laser pulses over large distances.

In Sec. IV, the results of simulation for short, intense

laser pulse propagation in capillaries with parameters achievable with existing laser systems are presented and discussed. An example is given for aluminum capillary tubes, aluminum being a material whose properties are well documented. The structure of fields in the capillary and the properties of the plasma created at the inner surface of the capillary wall are presented for different parameters of laser pulses and capillary radius.

II. BASIC EQUATIONS

Let us consider a circularly polarized, axis-symmetric laser pulse propagating along the Oz axis from $z<0$ and impinging on a cylindrical capillary entrance at $z=0$:

$$\widetilde{\boldsymbol{E}} = \mathrm{Re}[\boldsymbol{E}\exp(-i\omega_0 t + ik_0 z + i\phi)],$$
$$\widetilde{\boldsymbol{B}} = \mathrm{Re}[\boldsymbol{B}\exp(-i\omega_0 t + ik_0 z + i\phi)], \tag{1}$$

where ω_0 and $k_0=\omega_0/c$ are respectively the frequency and the wave vector of the laser radiation in vacuum, ϕ is the azimuthal angle, and $\boldsymbol{E}(r,z,t)$ and $\boldsymbol{B}(r,z,t)$ are the complex amplitudes of the fields, slowly varying on the scales $1/\omega_0$ and $1/k_0$. In vacuum, just before the capillary tube entrance at $z=-0$, the vector structure of the incident fields is described by the laser pulse envelope in the radial direction, $F_\perp(r)$, and time, $F_\parallel(t)$:

$$\begin{Bmatrix}\boldsymbol{E}\\ \boldsymbol{B}\end{Bmatrix}(t,r,\phi,z=-0) = F(t)e^{i\phi}\begin{Bmatrix} i\\ 1\end{Bmatrix}\left[-i\boldsymbol{e}_r + \boldsymbol{e}_\phi + \boldsymbol{e}_z\frac{\partial}{\partial r}\right]F_\perp(r), \tag{2}$$

where $\boldsymbol{e}_r,\boldsymbol{e}_\phi$ and $\boldsymbol{e}_z$ are unit vectors; the upper and the lower rows here and below are for electric and magnetic field components, respectively.

Inside the capillary coaligned with the Oz axis, the laser pulse fields are taken in the form given by Eq. (1) with complex vector amplitudes

$$\boldsymbol{E} = \boldsymbol{e}_r E_r + \boldsymbol{e}_\phi E_\phi + \boldsymbol{e}_z E_z, \quad \boldsymbol{B} = \boldsymbol{e}_r B_r + \boldsymbol{e}_\phi B_\phi + \boldsymbol{e}_z B_z. \tag{3}$$

Using dimensionless variables comoving with the laser pulse,

$$\xi = k_0(z-ct), \quad \zeta = k_0 z, \quad \rho = k_0 r, \tag{4}$$

one can derive (see the Appendix for details) from Maxwell equations the following system of equations for the axial, azimuthal, and radial components of the fields (3):

$$\left[\Delta_\rho - \frac{1}{\rho^2} + 2i\frac{\partial}{\partial\zeta} + \varepsilon - 1 + 2\frac{\partial^2}{\partial\xi\,\partial\zeta}\right]\begin{Bmatrix}E_z\\ B_z\end{Bmatrix} + i\begin{Bmatrix}\varepsilon^{-1}[B_\phi - \rho^{-1}B_z]\\ -E_\phi + \rho^{-1}E_z + \partial_\rho B_z\end{Bmatrix}\frac{\partial_\rho\varepsilon}{\varepsilon} = 0, \tag{5}$$

$$\left[\varepsilon - 1 + 2i\frac{\partial}{\partial\zeta}\right]\begin{Bmatrix}E_\phi\\ B_\phi\end{Bmatrix} = i\begin{Bmatrix}-\partial_\rho B_z\\ \varepsilon\partial_\rho E_z\end{Bmatrix} - \frac{1}{\rho}\begin{Bmatrix}E_z\\ B_z\end{Bmatrix}, \tag{6}$$

$$\begin{Bmatrix}E_r\\ B_r\end{Bmatrix} = \begin{Bmatrix}\varepsilon^{-1}B_\phi\\ -E_\phi\end{Bmatrix} - \frac{1}{\rho}\begin{Bmatrix}\varepsilon^{-1}B_z\\ -E_z\end{Bmatrix}. \tag{7}$$

In these equations, $\Delta_\rho=\rho^{-1}\partial/\partial\rho+\partial^2/\partial\rho^2$; ε is the permittivity of the plasma, which is assumed to be a scalar function, depending on the local plasma properties at a given point.

For wide enough capillaries, when the inner radius R_0 is much larger than the laser wavelength $\lambda_0=2\pi/k_0$:

$$k_0 R_0 \gg 1, \tag{8}$$

and for short laser pulses, the system of Eqs. (5) and (6) can be simplified substantially when the characteristic length of plasma expansion during the pulse due to the heating of the capillary walls, δR_{exp}, is much smaller than the laser wavelength:

$$k_0\delta R_{\mathrm{exp}} \ll 1, \tag{9}$$

with $\delta R_{\mathrm{exp}} \approx V_s\tau_L \sim \sqrt{ZT/m_i}\,\tau_L \approx 10\ \mathrm{nm}\cdot\tau_L(\mathrm{ps})\sqrt{ZT(\mathrm{eV})/\mathrm{A}}$, where τ_L is the laser pulse duration, Z and m_i are, respectively, the average charge and mass of plasma ions, T is the temperature of electrons, and A is the atomic weight; $\delta R_{\mathrm{exp}} \sim 10$ nm for typical parameters such as $Z\sim 10$, $T\sim 10^2$ eV, $\tau_L\sim 10^{-1}$ ps, and $A=27$.

For Eqs. (5)–(7) in the inner vacuum core, with conditions (8) and (9), the variation of the inner radius of the capillary due to plasma expansion can be neglected, as well as the temporal dependence of the expanding plasma boundary $R_{\mathrm{vac}}\cong R_0-\delta R_{\mathrm{exp}}\cong R_0$. For $r<R_{\mathrm{vac}}$ one can put $\varepsilon=1$ and rewrite Eqs. (5) and (6) as

$$\left[\Delta_\rho - \frac{1}{\rho^2} + 2i\frac{\partial}{\partial\zeta} + 2\frac{\partial^2}{\partial\xi\,\partial\zeta}\right]\begin{Bmatrix}E_z\\ B_z\end{Bmatrix} = 0, \tag{10}$$

$$2i\frac{\partial}{\partial\zeta}\begin{Bmatrix}E_\phi\\ B_\phi\end{Bmatrix} = i\begin{Bmatrix}-\partial_\rho B_z\\ \varepsilon\partial_\rho E_z\end{Bmatrix} - \frac{1}{\rho}\begin{Bmatrix}E_z\\ B_z\end{Bmatrix}. \tag{11}$$

Field equations inside the capillary walls, for $r\geqslant R_{\mathrm{vac}}$, can also be simplified. For such a simplification let us consider a region $r>R$ of expanding plasma, with R such that $R_{\mathrm{vac}}<R\leqslant R_0$, where the density of free electrons $n(r)$ is high enough to ensure the reflection of laser radiation. At the boundary of this region, $r=R$, which we call the effective plasma boundary, the following condition has to be satisfied:

$$n(R)/n_c \gg 1/(k_0R_0)^2, \tag{12}$$

where $n_c=m\omega_0^2/(4\pi e^2)$ is the critical density. This condition is equivalent to $n(R)/n_c \gg (k_\perp/k_0)^2$, where $k_\perp\sim 1/R_0$ is the characteristic transverse wave number of the field propagating inside the capillary for $r\leqslant R_{\mathrm{vac}}$. In the region $r\geqslant R$ only radial derivatives in Eqs. (5) and (6) are important, hence the equations for z and ϕ components of the fields have the following form:

$$\left[\frac{\partial^2}{\partial\rho^2} + \varepsilon - 1\right]\begin{Bmatrix}E_z\\ B_z\end{Bmatrix} - \frac{\partial_\rho\varepsilon}{\varepsilon - 1}\begin{Bmatrix}\varepsilon^{-1}\partial_\rho E_z\\ \partial_\rho B_z\end{Bmatrix} = 0, \tag{13}$$

$$\begin{Bmatrix} E_\phi \\ B_\phi \end{Bmatrix} = \frac{i}{\varepsilon - 1} \begin{Bmatrix} -\partial_\rho B_z \\ \varepsilon \partial_\rho E_z \end{Bmatrix}, \tag{14}$$

where ε depends on $|\boldsymbol{E}|^2 = |E_z|^2 + |E_r|^2 + |E_\phi|^2$ as the properties of the capillary wall are dependent on the absorbed laser energy.

The simplified Eqs. (10), (11), (13), and (14) allow to describe the fields in all the transverse dimensions except in a thin plasma layer $r \in [R_{\text{vac}}; R]$, where the density can be smaller than the critical density as imposed by conditions (12) and (8). For all the cases considered in this paper, the width of this thin, rarefied-plasma layer of thickness $\delta R_{\text{rar}} = R - R_{\text{vac}}$, is much less than the skin depth determined by the density at the boundary $r = R$, i.e.,

$$k_0 \delta R_{\text{rar}} \ll [n_c / n(R)]^{1/2}. \tag{15}$$

Therefore, the field variations as well as the laser pulse absorption in this layer can be safely neglected and the conditions of continuity of tangential fields components between the vacuum core $r \leqslant R_{\text{vac}}$ and the plasma region $r \geqslant R$ can be used at $r = R$:

$$\begin{aligned} &E_z|_{\rho=\mathcal{R}-0} = E_z|_{\rho=\mathcal{R}+0}, \quad B_z|_{\rho=\mathcal{R}-0} = B_z|_{\rho=\mathcal{R}+0}, \\ &E_\phi / B_z|_{\rho=\mathcal{R}-0} = \mu_B, \quad B_\phi / E_z|_{\rho=\mathcal{R}-0} = -\mu_E, \end{aligned} \tag{16}$$

where

$$\begin{aligned} &\mu_B = -i\chi_B / \sqrt{1 - \varepsilon_{\mathcal{R}}}, \quad \mu_E = -i\varepsilon_R \chi_E / \sqrt{1 - \varepsilon_{\mathcal{R}}}, \\ &\chi_B \equiv \left. \frac{-\partial_\rho \ln B_z}{\sqrt{1 - \varepsilon}} \right|_{\rho=\mathcal{R}+0}, \quad \chi_E \equiv \left. \frac{-\partial_\rho \ln E_z}{\sqrt{1 - \varepsilon}} \right|_{\rho=\mathcal{R}+0}, \end{aligned} \tag{17}$$

and designation $\rho = \mathcal{R} \mp 0$ stands for the points at the boundary of the vacuum core and of the plasma region, respectively; $\mathcal{R} \equiv k_0 R$ and $\varepsilon_{\mathcal{R}} \equiv \varepsilon(\mathcal{R} + 0)$; the coefficients χ_B and χ_E are equal to 1 for the case of a step-like plasma profile, homogeneous for $r \geqslant R$.

As the width of the neglected rarefied plasma layer δR_{rar} is smaller by definition than the scale length of plasma expansion δR_{exp}, the criterion (15) is less restrictive than condition (9), which is satisfied in a wide range of intensities for subpicosecond pulses propagating in wide capillaries under condition (8).

So finally we solve Eqs. (10) and (11) for $r \leqslant R$ and Eqs. (13) and (14) for $r \geqslant R$ with the boundary conditions (16) and (17) at the effective plasma boundary, $r = R$, satisfying conditions (12) and (15), and being a function of ζ and ξ. For the results presented below the effective boundary position, R, was defined by the relation $n(R)/n_c = 0.3$ and it was checked that the results do not depend on the particular value of the ratio $n(R)/n_c$ as long as it satisfies conditions (12) and (15).

Equations (10) and (13) have been solved using the additional boundary conditions of nonsingularity of fields at $r \to 0$ and of their asymptotic attenuation at $r \to \infty$:

$$E_z(r \to 0) = O(r), \quad B_z(r \to 0) = O(r), \tag{18}$$

$$E_z \underset{r\to\infty}{\to} 0, \quad B_z \underset{r\to\infty}{\to} 0. \tag{19}$$

For $r \leqslant R$, an approximate analytical solution of Eqs. (7), (10), and (11) can be found by writing the fields in terms of quasimodes:

$$\begin{Bmatrix} \boldsymbol{E} \\ \boldsymbol{B} \end{Bmatrix} = A_{\max} \sum_{n=1}^{N} \mathfrak{C}_n \begin{Bmatrix} \boldsymbol{E}_n(\rho) \\ \boldsymbol{B}_n(\rho) \end{Bmatrix} X_n(\xi, \zeta) \times \exp\left[-i \int_0^\zeta k_{\perp n}^2(\xi, \zeta) d\zeta / 2 \right], \tag{20}$$

where $A_{\max} \equiv \sqrt{4\pi I_L / c}$ is the maximum amplitude of the field and $k_{\perp n}$ is the dimensionless, transverse wave vector normalized to k_0. As will be shown in Sec. IV, only a few modes contribute significantly to the fields, so that the maximum number N of modes in Eq. (20) can be restricted to a few units, and we can assume that $k_{\perp N} \sim N/(k_0 R_0) \ll 1$. The coefficients of expansion $\mathfrak{C}_n$ and $X_n(\xi, \zeta = +0)$ are determined by the boundary conditions at the capillary entrance $z = +0$, while boundary conditions (16) and (17) induce a weak dependence of the radial functions $\boldsymbol{E}_n(\rho) = \boldsymbol{e}_z E_{z,n} + \boldsymbol{e}_r E_{r,n} + \boldsymbol{e}_\phi E_{\phi,n}$ and $\boldsymbol{B}_n(\rho) = \boldsymbol{e}_z B_{z,n} + \boldsymbol{e}_r B_{r,n} + \boldsymbol{e}_\phi B_{\phi,n}$ on ξ and ζ.

The transverse and longitudinal structures of quasimodes in vacuum are determined at the first order of the small parameter $(k_0 R_0)^{-1}$ from the following equations:

$$[\Delta_\rho - 1/\rho^2 + k_{\perp n}^2] \begin{Bmatrix} E_{z,n} \\ B_{z,n} \end{Bmatrix} = 0, \tag{21}$$

$$\frac{1}{k_{\perp n}^2} \left[-\frac{1}{\mathcal{R}} \begin{Bmatrix} E_{z,n}/B_{z,n} \\ B_{z,n}/E_{z,n} \end{Bmatrix} + i \begin{Bmatrix} -\partial_\rho \ln B_{z,n} \\ \partial_\rho \ln E_{z,n} \end{Bmatrix} \right]_{\rho=\mathcal{R}-0} = \begin{Bmatrix} \mu_B \\ -\mu_E \end{Bmatrix}, \tag{22}$$

$$\begin{Bmatrix} E_{\phi,n} \\ B_{\phi,n} \end{Bmatrix} = \frac{-1}{k_{\perp n}^2} \left[i\partial_\rho \begin{Bmatrix} B_{z,n} \\ E_{z,n} \end{Bmatrix} + \rho^{-1} \begin{Bmatrix} E_{z,n} \\ B_{z,n} \end{Bmatrix} \right], \tag{23}$$

$$[\partial_\zeta - (k_{\perp n}^2/2)\partial_\xi - i\partial_\zeta \partial_\xi] X_n = 0. \tag{24}$$

The fields in the whole space, at the first order of $(k_0 R_0)^{-1}$, can then be written as

$$E_{z,n} = -i \times \begin{cases} \mathfrak{J}_1(\rho), & \rho < \mathcal{R}, \\ \mathfrak{J}_1(\mathcal{R}) G_E(\rho), & \rho \geqslant \mathcal{R} \end{cases},$$

$$\mathfrak{J}_1(\rho) \equiv \frac{u_n}{\mathcal{R}} J_1(u_n \rho / \mathcal{R}), \tag{25}$$

$$B_{z,n} = -\begin{cases} \mathfrak{J}_1(\rho), & \rho < \mathcal{R}, \\ \mathfrak{J}_1(\mathcal{R}) G_B(\rho), & \rho \geqslant \mathcal{R} \end{cases},$$

$$E_{\phi,n} = i \times \begin{cases} J_0(u_n\rho/\mathcal{R})[1 + i\mu^- u_n^2/\mathcal{R}] + i\mathfrak{J}_1(r)[\mu^+\rho/\mathcal{R} - \mu^-\mathcal{R}/\rho], & \rho < \mathcal{R}, \\ -\mathfrak{J}_1(\mathcal{R})[1-\varepsilon]^{-1}\partial_\rho G_B(\rho), & \rho \geqslant \mathcal{R} \end{cases},$$

$$B_{\phi,n} = \begin{cases} J_0(u_n\rho/\mathcal{R}) + i\mathfrak{J}_1(\rho)[\mu^+\rho/\mathcal{R} + \mu^-\mathcal{R}/\rho], & \rho < \mathcal{R}, \\ -\mathfrak{J}_1(\mathcal{R})\varepsilon[1-\varepsilon]^{-1}\partial_\rho G_E(\rho), & \rho \geqslant \mathcal{R}, \end{cases} \quad (26)$$

$$\begin{Bmatrix} E_{r,n} \\ B_{r,n} \end{Bmatrix} = \begin{Bmatrix} \varepsilon^{-1}B_{\phi,n} \\ -E_{\phi,n} \end{Bmatrix}, \quad (27)$$

where u_n is the n-th root of the zero-order Bessel function J_0, J_1 is the first-order Bessel function, and

$$\mu^{\pm} = (\mu_E \pm \mu_B)/2. \quad (28)$$

The functions G_B and G_E, which describe the field structure in the plasma region $r > R$, are the normalized solutions to Eqs. (13) with boundary conditions

$$G_E(\rho = \mathcal{R}) = G_B(\rho = \mathcal{R}) = 1; \quad G_E \underset{r\to\infty}{\to} 0, \quad G_B \underset{r\to\infty}{\to} 0. \quad (29)$$

The eigenvalues of the normalized longitudinal and transverse wave vectors can be expressed as

$$k_n \cong 1 - k_{\perp n}^2/2 \cong 1 - u_n^2/[2\mathcal{R}^2] + i\mu^+ u_n^2/\mathcal{R}^3,$$
$$k_{\perp n} = (u_n/\mathcal{R})[1 - i\mu^+/\mathcal{R}]. \quad (30)$$

Note that for a *homogeneous* capillary wall with constant ε, $\mu^+ = -(i/2)(1+\varepsilon_R)/\sqrt{1-\varepsilon_R}$. In this case $1/\mu^+$ corresponds to the "effective wave vector" introduced in Ref. 11 and Eqs. (25) and (26) coincide, after respective transformation of variables, with the results of Ref. 9.

In Eq. (20), the coefficients $\mathfrak{C}_n$ are determined by the transverse structure of the incident laser pulse (2) at the capillary entrance $z = +0$ (see also Ref. 12):

$$\mathfrak{C}_n = \frac{2}{J_1^2(u_n)} \int_0^1 x J_0(u_n x) F_\perp(x) dx, \quad x \equiv \rho/\mathcal{R}. \quad (31)$$

The time envelope of the incident laser pulse (2) determines the boundary conditions at $z = 0$ for Eq. (24):

$$X_n(\xi, \zeta = +0) = F(\xi), \quad (32)$$

which gives the following approximate solutions:

$$X_n(\xi,\zeta) = F\left(\xi + \frac{1}{2}\int_0^\zeta k_{\perp n}^2(\zeta')d\zeta'\right), \quad (33)$$

obtained for laser pulse durations much longer than the laser period, $\omega_0\tau_L \gg 1$.

In order to determine the dielectric permittivity entering the field equations, it is necessary to model the dynamics of the plasma under the action of the energy flux of the laser at the capillary wall. In the numerical simulations presented in Sec. IV, two temperature hydrodynamic equations including ionization dynamics and inverse bremsstrahlung absorption of laser radiation were used for plasma dynamics.[13] The time evolution of the capillary wall at each distance of the laser pulse propagation z was calculated from the initial conditions of a metal at room temperature with a sharp boundary at $r = R_0$ and $\xi \to \infty$.

The inverse bremsstrahlung absorption rate, which is the source of heating for the electron component of the created plasma,[13] can be expressed as follows:

$$Q_{IB} = \omega_0 \frac{|\boldsymbol{E}|^2}{8\pi} \mathrm{Im}\{\varepsilon\} = \frac{I_L}{2k_0R^2}\Sigma_{\mathrm{modes}}\left[\left|\frac{\partial G_B/\partial\rho}{1-\varepsilon}\right|^2 + |G_E|^2 + \left|\frac{\partial G_E/\partial\rho}{1-\varepsilon}\right|^2\right]\mathrm{Im}\{\varepsilon\}, \quad (34)$$

$$\Sigma_{\mathrm{modes}} \equiv \left|\sum_{n=1}^N \exp\left\{i\int k_n(\xi,\zeta)d\zeta\right\} u_n J_1(u_n)\mathfrak{C}_n X_n(\xi,\zeta)\right|^2. \quad (35)$$

III. DESCRIPTION OF PLASMA DYNAMICS

The description of ionization, heating, and expansion of the plasma, created at the capillary walls under the effect of the transverse energy flux, is based on the system of hydrodynamical equations for the total concentration of atoms and ions n_a or density of plasma $\varrho_a = m_i n_a$, average charge of ions Z, velocity of quasineutral plasma V in the transverse direction r, and energy per particle of electrons U^e and ions U^i:

$$\frac{\partial\varrho_a}{\partial t} + \frac{\partial(\varrho_a V)}{\partial r} = 0, \quad (36)$$

$$\left[\frac{\partial}{\partial t} + V\frac{\partial}{\partial r}\right]V = -\frac{1}{\varrho_a}\frac{\partial}{\partial r}[P_e + P_i] - K_1\left(\frac{3\sqrt{\pi}}{4}\frac{\nu_{\mathrm{eff}}}{\omega_0}\right)\frac{Zm}{4m_i}\frac{\partial|\boldsymbol{V}_E|^2}{\partial r}, \quad (37)$$

$$n_a\left[\frac{\partial}{\partial t} + V\frac{\partial}{\partial r}\right]U^i = -P_i\frac{\partial}{\partial r}V + Q^{\{e-i\}}, \quad (38)$$

$$Zn_a\left[\frac{\partial}{\partial t} + V\frac{\partial}{\partial r}\right]U^e = -\frac{\partial}{\partial r}q_T - P_e\frac{\partial}{\partial r}V - Q^{\{e-i\}} - Q_{\mathrm{rad}} - Q_Z + Q_{IB} - U^e\Theta, \quad (39)$$

$$n_a\left[\frac{\partial Z}{\partial t}+V\frac{\partial}{\partial r}Z\right]=\Theta, \tag{40}$$

where P_e and P_i are, respectively, electronic and ionic pressure, $Z=n_a^{-1}\Sigma_{q=1}^{z_n}qn_q$ is the average charge of ions, $n_a=\Sigma_{q=0}^{z_n}n_q$, n_q is the concentration of ions with charge q, z_n is the charge of nucleus; Θ is the total rate of thermal ionization; $V_E\equiv e|\mathbf{E}|/[m\omega_0]$ is the amplitude of the quiver velocity of electrons in the laser field; ν_{eff} is the effective frequency of electron-ion collisions; the function

$$K_1(x)=\frac{8}{3\sqrt{\pi}}\int_0^\infty\frac{t^{10}e^{-t^2}}{t^6+x^2}dt,$$

Q_{IB} is determined by (34);

$$Q^{\{e-i\}}=3\frac{m}{m_i}Zn_a\nu_{\text{eff}}(T-T^i)$$

is the density of power, transmitted from electrons to ions during collisions (electron-ion relaxation), T^i is the ion temperature;

$$q_T=-\frac{128}{3\pi}\kappa_Z\frac{Zn_aT}{m\nu_{\text{eff}}}\frac{\partial T}{\partial r}$$

is the electronic thermal flux, $\kappa_Z=[1+4.79/Z-6.02/Z^2+9.13/Z^3-4.65/Z^4]^{-1}$ is a multiplier, which takes into account the influence of electron-electron collisions on the thermoconductivity;

$$Q_{\text{rad}}=\frac{4e^2}{\sqrt{3}\hbar c}\frac{T^2}{mc^2}Zn_a\nu_{\text{eff}} \tag{41}$$

is the estimate of energy losses due to bremsstrahlung thermal radiation;

$$Q_Z=n_a\left[\frac{\partial}{\partial t}+V\frac{\partial}{\partial r}\right]\mathfrak{E}_I,\quad \mathfrak{E}_I=\sum_{q=1}^{z_n}\frac{n_q}{n_a}\sum_{k=1}^{q}U_k, \tag{42}$$

where Q_Z is the density of power absorbed due to thermal ionization (or emitted due to recombination) and $\mathfrak{E}_I$ represents the energy spent for thermal ionization, U_q is the potential of q-fold ionization.

The system of Eqs. (36)–(40) was solved using a one-dimensional (1D) Lagrangian code; finite-difference implicit schemes with Newton iterations were used for solving equations (36), (37), and (39).

Taking into account only *collisional* ionization and recombination and using the approximation of average ion, one can write the following expressions for the total speed of thermal ionization Θ, the density of power Q_Z and the energy spent $\mathfrak{E}_I=\int_{Z_{\min}}^{Z}U_{n_I(Z)}(Z)dZ$ for thermal ionization:[13,14]

$$\Theta=Zn_a^2\kappa(Z)[1-Z/Z_{\text{eq}}], \tag{43}$$

$$\kappa(Z)\approx 6\times 10^8\frac{\text{cm}^3}{\text{s}}\sum_{n=1}^{3}L_n(Z)\sqrt{\frac{U_H}{T}}\frac{U_H}{U_n}e^{-U_n/T}f\left(\frac{U_n}{T}\right),$$

$$L_n(Z)=2n^2\mathcal{Q}\left(\frac{z_n-M_{n-1}-Z}{2n^2}\right),$$

$$U_n(Z)=[z_n-M_{n-1}-L_n(Z)+1]^2\frac{U_H}{n^2}, \tag{44}$$

$$Q_Z=U_{n_I}(Z)\Theta+n_a\frac{\partial V}{\partial r}\frac{U_H}{9}(Z_{\min}+1)^2n_a\frac{\partial Z_{\min}}{\partial n_a},$$

$$\mathfrak{E}_I=\frac{U_H}{3}\begin{cases}\frac{1}{9}[(Z+1)^3-(Z_{min}+1)^3], & n_I=3\Leftrightarrow Z<z_n-M_2,\\ \frac{1}{9}[(z_n-M_2+1)^3-(Z_{min}+1)^3] & \\ +\frac{1}{4}[(Z+1)^3-(z_n-M_2+1)^3], & n_I=2\Leftrightarrow z_n-M_2<Z<z_n-M_1,\\ \frac{1}{9}[(z_n-M_2+1)^3-(Z_{min}+1)^3] & \\ +\frac{1}{4}[(z_n-M_1+1)^3-(z_n-M_2+1)^3] & \\ +[(Z+1)^3-(z_n-M_1+1)^3], & n_I=1\Leftrightarrow z_n-M_1<Z,\end{cases} \tag{45}$$

where $n_I=n_I(Z)$ is the number of the shell where ionization takes place; $Z_{\text{eq}}=Z_{\text{eq}}(n_a,T)$ is the equilibrium average ion charge at given temperature and density of plasma, determined according to More's[15] quasistationary formula, $Z_{\min}=Z_{\text{eq}}(n_a,T=0)$ is the minimum average charge of ions; L_n is the number of electrons in the shell with principal quantum number n, M_n is the number of electrons in closed electronic shells ($M_n=0,2,10,18,\ldots$ for $n=0,1,2,3,\ldots$, respectively), U_n is the potential of ionization of the shell number n in a "hydrogen-like" approximation, U_H is the potential of ioniza-

tion of hydrogen; $\mathcal{Q}(x)$ is a function equal to zero for $x<0$, to unity for $x>1$, and to x for $x\in[0;1]$; the function f is determined as

$$f(x)\approx \ln\left[1+\frac{1+2.5x}{1.78x(1+1.4x)}\right].$$

The formula (45) is written for the case of no more than three shells in the atom, which corresponds to $z_n\leqslant 18$.

For the determination of the effective collision frequency and plasma permittivity, let us note that at high electron temperature ($\gtrsim 10^2$ eV for a solid-density plasma) the electron component of the plasma can be treated in an ideal nondegenerate gas approximation. In this case the effective frequency of electron-ion collisions can be written as

$$\nu_{\text{eff}}=4\sqrt{2\pi}nZe^4\Lambda/[3\sqrt{m}T^{3/2}], \tag{46}$$

where

$$\Lambda=\ln[1+(3/\Gamma_D)^3],\quad \Gamma_D=Ze^2/(r_{De}T),\quad \text{and}$$

$$r_{De}=\sqrt{T/(4\pi ne^2)}$$

are the Coulomb logarithm for weakly coupled plasma, Debye parameter of coupling, and the Debye radius, respectively. Under the same approximation the permittivity is

$$\varepsilon=1-\frac{n}{n_c}\left[K_1\left(\frac{3\sqrt{\pi}}{4}\frac{\nu_{\text{eff}}}{\omega_0}\right)-i\frac{\nu_{\text{eff}}}{\omega_0}K_2\left(\frac{3\sqrt{\pi}}{4}\frac{\nu_{\text{eff}}}{\omega_0}\right)\right], \tag{47}$$

where

$$K_2(x)=2\int_0^\infty \frac{t^7e^{-t^2}}{t^6+x^2}dt.$$

At low temperatures $T\lesssim 34$ eV$(n_a/6\ 10^{22}\ \text{cm}^{-3})\times(Z/10)^{5/6}$ the mean free path of electrons becomes lower than the mean distance between ions. Under such conditions the effective frequency should be restricted to the value[13,16]

$$\nu_{\text{eff,max}}=\omega_{pe}/\sqrt{6}, \tag{48}$$

where $\omega_{pe}=\sqrt{4\pi ne^2/m}$ is the plasma frequency. At lower temperatures $T<T_F=[3\pi^2n]^{2/3}\hbar^2/[2m]$, where T_F is the Fermi temperature, one can use the following expression for the effective collision frequency in metallic plasma:[17,18]

$$\nu_{\text{eff}}\approx \nu_0[1+T^2/(T_FT^i)],\quad \nu_0\sim T^i/\hbar\ , \tag{49}$$

where ν_0 is the electron-phonon collision frequency. For the intensity range considered here, the contribution of interband absorption[17] was not taken into account; it can have a significant contribution in a narrow range close to room temperature.

In numerical calculations the effective frequency was defined as the minimum of the values given by Eqs. (46), (49), and (48). This approach, though rather elementary, still gives adequate results when compared to more sophisticated approaches.[13,19]

The plasma permittivity at $T\leqslant T_F$ was determined by the Drude formula:[17]

$$\varepsilon=1-\frac{(n/n_c)}{[1+i(\nu_{\text{eff}}/\omega_0)]}, \tag{50}$$

with ν_{eff} determined by Eq. (49).

In numerical simulations an interpolation between Eqs. (47) and (50) in the region $T\gtrsim T_F$ was used. The center of the region of temperatures, where Eqs. (47) and (50) were connected, was determined by the condition of equivalence of expressions (49) and (46).

For ultraintense laser pulses the electromagnetic field strength can be high even near the capillary wall. The possible decrease of collision frequency in high-frequency intense electromagnetic fields is taken into account by replacing the value ν_{eff} by the value $\nu_{\text{eff}}\kappa_L$, where

$$\kappa_L=1-0.553\{1+(1.08/Z)|V_{Te}/V_E|^2[1+(\nu_{\text{eff}}/\omega_0)^2]^{3/4}\}^{-1} \tag{51}$$

is the Langdon correction factor,[20] $V_{Te}\equiv\sqrt{T/m}$.

The electron energy is interpolated by the expression

$$U^e\approx U_m^eU_p^e/\sqrt[3]{(U_m^e)^3+(U_p^e)^3},\quad \text{where}$$

$$U_p^e=3T/2,\ U_m^e=(\pi^2/4)T^2/T_F, \tag{52}$$

which gives correct values for degenerate and nondegenerate cases. For ion energy, and ion and electron pressures, ideal gas expressions were used. As long as the laser energy is absorbed mainly by electrons and the electron-ion relaxation time is much longer than 1 ps, the inaccuracy of those simple equations of states does not lead to noticeably different results from those calculated by means of more sophisticated equations of states.[21]

IV. SIMULATION RESULTS

The results of simulations presented in this section describe the propagation of short, intense circularly polarized laser pulses inside an aluminum capillary tube with inner radius $R_0=25$ μm. The incident laser pulse (2) is assumed to be Gaussian in the longitudinal and transverse directions:

$$F(t)=\exp[-2\ln 2(t/\tau_L)^2], \tag{53}$$

$$F_\perp(r)=\exp[-(r/r_0)^2]. \tag{54}$$

For all the examples given below, the laser wavelength is $\lambda_0=0.8$ μm; the initial pulse duration, full width at half maximum (FWHM) of the intensity, is $\tau_L=35$ fs for Figs. 1–3, $\tau_L=35$ or 350 fs for Fig. 5, and $\tau_L=350$ fs for Fig. 4.

A. Properties of the fields inside the capillary tube

Figure 1 illustrates the properties of the laser pulse propagation along the capillary axis Oz in the case of $r_0=16$ μm, with a ratio $r_0/R_0=0.637$, which corresponds to the condition of best matching of the incident Gaussian pulse to the first eigenmode of the capillary tube, i.e., when the maximum amount of incident energy ($\cong 98\%$) is coupled to the first mode. The distance z along the capillary axis is normalized to the Rayleigh length $Z_R=k_0r_0^2/2=1$ mm. The maxi-

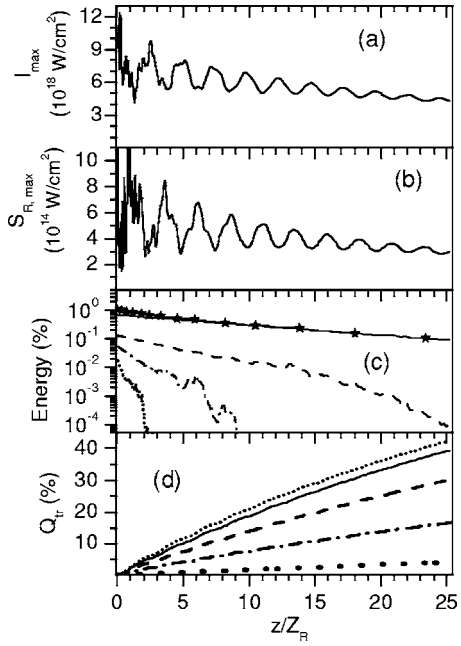

FIG. 1. Distributions along the capillary length z, normalized to the Rayleigh length $Z_R=1$ mm, of (a) the maximum laser energy flux $I_{\max}=\max_{\xi}[S_z(r=0)]$; (b) the maximum transverse flux into the wall $S_{R,\max}=\max_{\xi}[S_r(r=R)]$; (c) the values (in %) of $100-Q_1$ (line with markers), Q_2 (solid line), Q_3 (dashed line), Q_5 (dashed-dotted line), and Q_9 (dotted line), where $Q_n, n=1,2,\ldots$ is the part of the total energy contained in the n-th mode; and (d) the part of laser energy (in %) transmitted to the wall. The maximum intensity is $I_L=10^{19}$ W/cm^2 for all lines in (a)–(c) and solid and dotted lines in (d); $I_L\to 0$, $I_L=10^{17}$ W/cm^2, and $I_L=10^{18}$ W/cm^2 for short dashed, dashed-dotted, and dashed lines, respectively, in (d); the dotted line in (d) stands for the case $I_L=10^{19}$ W/cm^2 without expansion ("frozen" ions). The laser pulse radius $r_0=16$ μm.

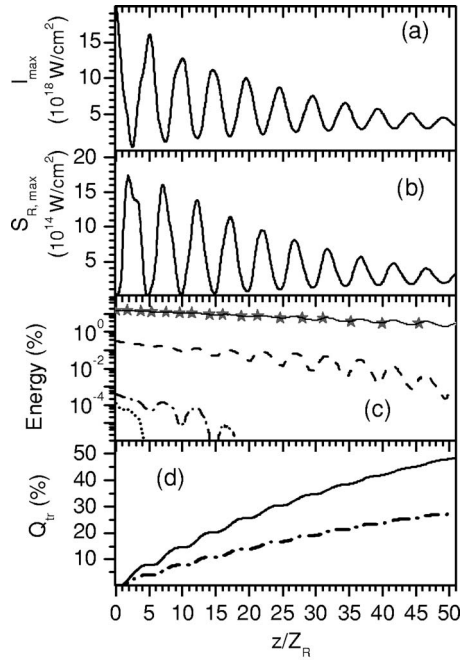

FIG. 2. Same as Fig. 1 for a laser pulse radius $r_0=11.3$ μm ($Z_R=0.5$ mm) and $I_L=2\times 10^{19}$ W/cm^2.

mum intensity on the laser axis before the entrance into the capillary is equal to $I_L=10^{19}$ W/cm^2 in Figs. 1(a)–1(c) and is in the range $0-10^{19}$ W/cm^2 in Fig. 1(d). The energy of the laser pulse is $\mathcal{E}=1.5$ J in Figs. 1(a)–1(c) and in the range 0 -1.5 J in Fig. 1(d). In Fig. 2 are plotted the same quantities as in Fig. 1 for the case of an unmatched pulse radius. The radius is reduced by a factor of $\sqrt{2}$ ($r_0/R_0=0.450$) keeping the same value for the total energy $\mathcal{E}=1.5$ J; $I_L=2\times 10^{19}$ W/cm^2.

In Figs. 1(a), 1(b), 2(a), and 2(b) are plotted the longitudinal (and transverse) fluxes; Figs. 1(c) and 2(c) present the percentage of total energy in the n-th mode Q_n. In Figs. 1(d) and 2(d) is plotted the fraction of laser pulse energy, $Q_{\rm tr}$, transmitted to the wall of the capillary for different peak intensities, $I_L\to 0$, $I_L=10^{17}$, $I_L=10^{18}$, and $I_L=10^{19}$ W/cm^2.

The transverse energy fluxes determine the properties of the plasma created at the capillary walls. The fluxes $I(r=0)=S_z(r=0)$ and $S_r(r=R)$, where I is the electromagnetic field intensity and S_z and S_r are the z and r components of the Poynting vector $\boldsymbol{S}=c(8\pi)^{-1}\,\mathrm{Re}\{\boldsymbol{EB}^*\}$, are calculated through the following expressions, derived from Sec. II:

$$S_r(R)=I_L\mathcal{R}^{-2}\Sigma_{\rm modes}\,\mathrm{Re}\{\mu^+\}, \tag{55}$$

where $\Sigma_{\rm modes}$ is given by (35),

$$S_z(0)=I_L\Sigma^z_{\rm modes},$$
$$\Sigma^z_{\rm modes}=\left|\sum_{n=1}^{N}\exp\{i\int k_n(\xi,\zeta)d\zeta\}\mathfrak{C}_nX_n(\xi,\zeta)\right|^2. \tag{56}$$

We can observe in Figs. 1(a), 1(b), 2(a), and 2(b) oscillations of energy fluxes along the capillary length z, with maxima of transverse flux corresponding to minima of intensity on the capillary axis. These oscillations are produced by the interference between the modes entering Eq. (20). High order modes are generated either at the entrance of the capillary tube through the diffraction of the incoming pulse, or inside the tube due to the nonlinearity of the boundary conditions. On the other side, these modes are damped during propagation by absorption into the capillary walls. The damping being governed by the imaginary part of the wave vector k_n [Eq. (30)] the highest order modes have the largest damping coefficient. The curves of Figs. 1(a), 1(b), 2(a), and 2(b) exhibit two domains:

- First, close to the entrance of the tube, at $z\leqslant 3Z_R$, the oscillations can have a complicated structure and a high amplitude because of the relatively high amount of energy contained in the higher order modes generated by diffraction, as can be seen in Fig. 1(c). Diffraction has a larger contribution in Figs. 1(a) and 1(b) than in Figs. 2(a) and 2(b) because of the larger radius of the focal spot in the former case, that is why curves in Figs. 1(a) and 1(b) exhibit the more complicated oscillations with higher frequencies.
- Second, for $z>3Z_R$, the amplitude of modes with $n>2$ drops below 1% and the first two modes dominate in the capillary at high z, as can be seen in Fig. 1(c).

The relative contribution of each of these modes is nearly constant because nonlinearities counterbalance a large part of the damping.

At high z, taking into account only the first two modes, and neglecting their attenuation and the variation of their envelope due to dispersion, one can obtain from (56) the following simple estimate for the position, $z_{\min,n}$, of the n-th minimum of the longitudinal flux along the capillary length z:

$$\frac{z_{\min,n}}{Z_R} = \left(\frac{R_0}{r_0}\right)^2 \frac{8\pi}{u_2^2 - u_1^2}(n+1/2) \approx 1.018\left(\frac{R_0}{r_0}\right)^2 (n+1/2). \tag{57}$$

According to (57), the distance between minima of the intensity on axis is $\approx 2.5 Z_R$ under the conditions of Fig. 1(a) and $\approx 5 Z_R$ under the conditions of Fig. 2(a), which is very close to the numerical results.

The total energy of the laser field decreases due to energy losses into capillary walls, as shown in Fig. 1(d). The relative energy loss increases dramatically with increasing intensity due to the modification of the wall properties, indicating that the propagation of intense laser pulses in thin capillary wave guides is strongly nonlinear. The comparison of solid and dotted curves in Fig. 1(d) shows that the process of hydrodynamic expansion of capillary walls is not very important for short ($\tau_L < 100$ fs) laser pulses at intensities $I_L \leqslant 10^{19}$ W/cm^2. Wall ionization and heating are dominant in this case.

From Fig. 2(a), we observe that the oscillations are much deeper than in the case of best matching; that corresponds to a larger amount of energy contained in the second mode, as seen in Fig. 2(c).

The present study was devoted to the case of metallic capillaries. For dielectric capillaries, it is expected that for high intensity laser pulses, the physical picture will be similar due to the transition of the dielectric to a metal and then to a plasma by the absorption of the laser flux. Nevertheless, at the front of the laser pulse the medium remains in a dielectric state, which could lead to higher laser energy losses than in the case of metallic capillaries, because of the leakage of laser field through the transparent walls of a dielectric. But for the global energy losses, the difference between metallic and dielectric capillaries is not expected to be large for intense laser pulses, as long as the central part of the pulse, where the energy losses are the most important, will propagate in both cases under conditions of hot plasma, created at capillary walls.

B. Properties of the plasma created at the capillary walls

The front of the laser pulse encounters conditions of cold, unchanged walls, while the center and the back of the pulse interact with heated walls. In order to examine the walls and fields evolution from the front to the tail of the laser pulse, the transverse energy flux and the quantities characterizing the properties of the capillary walls are plotted in Fig. 3 as a function of the local time ξ for different positions z along the capillary length (solid curves $z/Z_R = 6.0$, dashed curves $z/Z_R = 7.2$, and dotted curves $z/Z_R = 25$) for the case of best matching and an intensity $I_L = 10^{19}$ W/cm^2. For the same pulse energy, but under conditions far from best matching, the results are qualitatively similar.

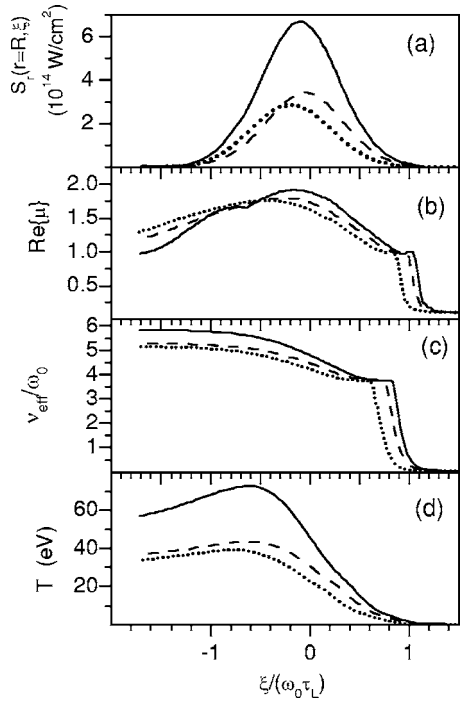

FIG. 3. Dependence on the local time $\xi = k_0(z - ct)$ of (a) the transverse energy flux at the plasma boundary $r = R$; (b) Re$\{\mu^+\}$; (c) the ratio of the effective electron collision frequency to the laser frequency $\nu_{\text{eff}}/\omega_0$; and (d) the electron temperature at $r = R$ for $z/Z_R = 6.0$ (solid curves), $z/Z_R = 7.2$ (dashed curves), and $z/Z_R = 25$ (dotted curves). The parameters are the same as in Fig. 1 for $I_L = 10^{19}$ W/cm^2.

Figure 3(a) shows, in accordance with Fig. 1(b), that the maximum value of the transverse energy flux decreases for increasing z. The position of the maximum flux moves with increasing z to the left from the point $\xi = 0$ due to dispersion, and the longitudinal envelop is almost Gaussian in agreement with expression (33).

From expression (55) it can be seen that the properties of the capillary wall determine the transverse energy flux into the wall through the real part of μ^+ [Eq. (28)] plotted in Fig. 3(b). The sharp increase of μ^+ at the front of the laser pulse is connected with the sharp increase of the electron collision frequency, shown in Fig. 3(c), which, in turn, is related to the increase of electron temperature exhibited in Fig. 3(d). This increase in Re$\{\mu^+\}$ from the "cold" value ≈ 0.13 up to the "hot" value $\approx 1-2$ is responsible for the increase of energy losses, in comparison with the case of low-intensity laser pulses [short-dashed line in Fig. 1(d)]. The subsequent slow evolution of Re$\{\mu^+\}$ is connected mainly with variations of electron density due to the expansion and ionization of the material of the capillary wall.

A typical example of the plasma transverse characteristics along the coordinate r, counted from the initial capillary radius $R_0 = 25$ μm, is shown in Fig. 4 for the length $z = 6Z_R$ at a time corresponding to $\xi = -0.5 c\tau_L$, which is approxi-

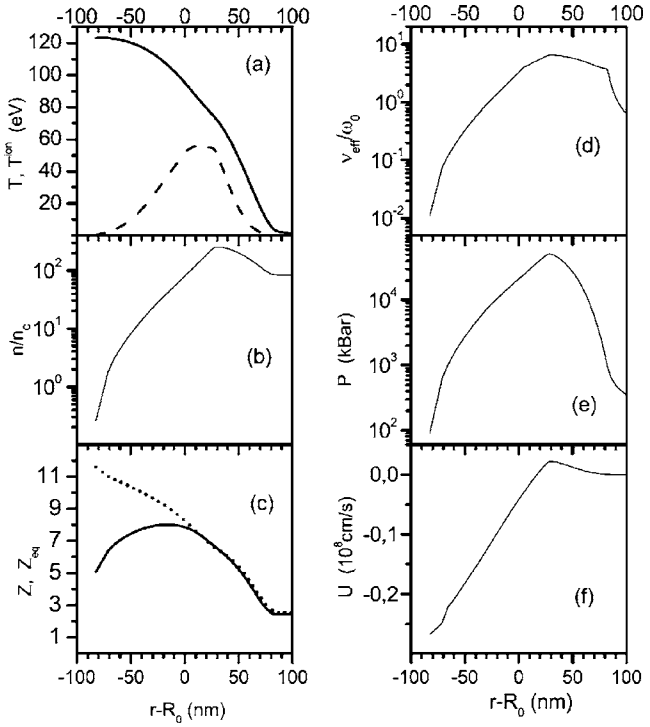

FIG. 4. Space distributions along the transverse coordinate r with origin R_0 of (a) the electron temperature T (solid curve) and the ion temperature T^{ion} (dashed curve), (b) the electron concentration normalized to the critical one, n/n_c, (c) the average ion charge z (solid curve) and equilibrium average ion charge (dotted curve), (d) the electron collision frequency normalized to the laser frequency $\nu_{\text{eff}}/\omega_0$, (e) the electron pressure, and (f) the quasineutral plasma velocity U, at the distance $z=6Z_R$; $\xi=-0.5c\tau_L$. $I_L=10^{19}$ W/cm^2, $\tau_L=350$ fs, and all other parameters are the same as for Fig. 1.

mately the time when the electron temperature reaches a maximum. The intensity is $I_L=10^{19}$ W/cm^2 and the duration $\tau_L=350$ fs.

From Fig. 4(a) it is seen that the electron temperature is much larger than the ion one, especially in the region $r<R_0$ of expanded plasma. This is due to the fact that the rate for energy exchange is proportional to the square of the density. In Fig. 4(c) we observe that for $r<R_0$ the average ion charge has a much lower value than the equilibrium one, hence ionization through electron-ion collision will induce a cooling of the electrons in this region. The width of the plasma domain, close to $r=R$ and for which $n<n_c$ is of the order of 10 nm$\ll\lambda_0$ [Fig. 4(b)]. This small value validates the assumption made in Sec. II [inequality (15)].

In Fig. 4(e) is reported the distribution of electron pressure in the created plasma. Pressures of tens of Mbar are generated in the region of dense plasma near the original boundary of the capillary wall. Such high values of pressure lead to the formation of shock waves propagating inside the capillary wall, generating a peak of density at $r>R_0$ observed in Fig. 4(b) and also a peak of positive velocities (with maximum value $\sim$10 km/s) as seen in Fig. 4(f). The velocity of plasma expansion grows almost linearly with r and its characteristic rate is ~ 1 μm/10 ps.

C. Energy losses in the capillary walls

The relative energy losses Q_{tr} characterize the regime of propagation in a capillary. For relatively low maximum laser intensity, I_L, or short pulse duration, τ_L, the transverse flux at the capillary wall is below the threshold for plasma formation, the value of Q_{tr} is then entirely determined by the wall material and does not depend on I_L or τ_L. When the transverse flux becomes larger than the threshold, at higher values of I_L or τ_L, the situation is changed dramatically as shown in Fig. 5. In this figure, the energy losses Q_{tr} are plotted after propagation of laser pulses over the distance $z=1$ cm in an aluminum capillary, as functions of the peak intensities I_L for two pulse durations $\tau_L=35$ and 350 fs. The curve $Q_{\text{tr}}(I_L)$ exhibits a threshold between cold and hot behaviors, which is equal to $I_{\text{th}}\approx 3.5\times 10^{16}$ W/cm^2 for the case of $\tau_L=35$ fs and $I_{\text{th}}\approx 8\times 10^{15}$ W/cm^2 for the case of $\tau_L=350$ fs. An estimate for the value of this threshold can be found analytically. For low intensity and ultrashort ($\tau_L\lesssim 100$ fs) laser pulses the capillary wall is heated in the regime of volume heating, for which the length of thermal wave propagation is smaller or comparable to skin depth.[10] Taking into account only the electronic heating through inverse bremsstrahlung absorption (34) (expansion, ionization, ion heating, and all other processes are neglected) and using expressions (50) and (49) for the calculation of the permittivity of the plasma, we obtain, after a lengthy calculation, the value of the threshold peak intensity expressed as

$$I_{\text{th}} = 1.6 \times 10^{16}\ \text{W/cm}^2(\Xi k_\nu)^{-1}\left(\frac{\tau_L}{10\ \text{fs}}\right)^{-1}\left(\frac{\lambda_0}{1\ \mu\text{m}}\right)^{-4}\left(\frac{R_0}{10\ \mu\text{m}}\right)^{2}. \tag{58}$$

I_{th} is defined as the intensity at which the absorption coefficient of the transverse energy flux into a capillary walls, averaged over the laser pulse duration τ_L, becomes twice its value at $T=0$. In Eq. (58) the coefficient $\Xi=\Sigma_{n=1}^{3}u_n^2J_1^2(u_n)\mathfrak{C}_n^2$ is close to 1 for $r_0/R_0\in[0.3;0.55]$, while $\Xi\approx 1.2$ for the best matching ratio $r_0/R_0=0.637$ and Ξ rises from 1.2 to 1.66 for $r_0/R_0\in[0.64;0.75]$; the value of $k_\nu\equiv\hbar\nu_0/T^i$ is close to 3.3 for aluminum.[17] The threshold peak intensity given by (58) is equal to $I_{\text{th}}\approx 2\times 10^{16}$ W/cm^{2}for $\tau_L=35$ fs. The numerical value deduced from Fig. 5 is slightly higher $\approx 3.5\times 10^{16}$ W/cm^2, which is due to the fact that the thermoconductivity is taken into account in numerical calculations. In the case of longer pulses with $\tau_L=350$ fs the discrepancy between estimated ($I_{\text{th}}\approx 2\times 10^{15}$ W/cm^2) and numerically calculated ($I_{\text{th}}\approx 8\times 10^{15}$ W/cm^2) values of the threshold is higher, mainly because of the expansion of the plasma, which is not taken into account in the analytical estimation, but is significant for longer pulses even at $I_L\sim 10^{16}$ W/cm^2 (compare dashed and solid marked curves), and also because of the role of thermoconductivity.

The value of Q_{tr} increases with increasing laser intensity from its "cold" value $Q_{\text{cold}}\approx 1.6\,\%$ to a maximum value $Q_{\text{tr,max}}\approx 19\%$ for $I_L\approx 2\times 10^{19}$ W/cm^2 in the case of $\tau_L=35$ fs and $Q_{\text{tr,max}}\approx 13\%$ for $I_L\approx 3\times 10^{17}$ W/cm^2 in the

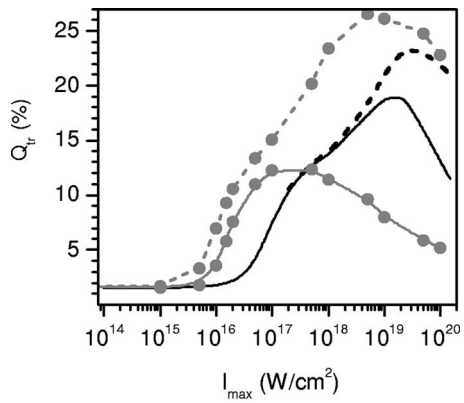

FIG. 5. Fraction of the laser energy (in %) transmitted to the wall at the capillary position $z=1$ cm as a function of the peak laser intensity at the entrance. The solid line is for the full calculation, and the dashed line for the case of "frozen" ions. $\tau_L=35$ (350) fs for lines without (with) markers. All other parameters are the same as in the case of Fig. 1.

case of $\tau_L=350$ fs. At still higher values of intensity, Q_{tr} becomes a decreasing function of I_L, which is connected with *i*) a strong influence of plasma expansion at the highest values of I_L and τ_L (compare solid and dashed curves in Fig. 5) and *ii*) the decrease of the effective electron-ion collision frequency with electron temperature T at high electron temperatures, $\nu_{\mathrm{eff}}\sim T^{-3/2}$ for $T\gtrsim 1.5\times 10^2$ eV for solid-density plasma.[13] The difference between solid and dashed curves in Fig. 5 indicates that the expansion of the plasma created at the wall plays a significant role, if $I_L>10^{19}$ W/cm^2 in the case of ultrashort (35 fs) pulses or if $I_L>10^{17}$ W/cm^2 in the case of longer (350 fs) pulses. For longer pulses the onset of expansion with increasing peak intensity occurs earlier than for shorter ones, which explains the fact that the maximum of the curve $Q_{\mathrm{tr}}(I_L)$ for $\tau_L=350$ fs is located at lower intensities, and that the value of this maximum is lower than in the case of $\tau_L=35$ fs (compare curves with and without markers in Fig. 5). Note that the values of intensities indicated above are given for the capillary radius $R_0=25$ μm and that they scale as the square of the capillary radius as the energy flux to the wall is inversely proportional to the square of the capillary radius [see Eqs. (55) and (58)].

V. CONCLUSION

A model describing the propagation of short intense laser pulses inside thin capillary waveguides, taking into account self-consistent ionization, heating, and expansion of capillary walls under the effect of the transverse energy flux and the backward influence of the properties of the created plasma on the evolution of laser fields inside the capillary, has been formulated. A hybrid electrohydroionization Lagrangian computer code has been developed to investigate self-consistently the processes of short intense ionizing laser pulses propagation in capillaries and plasma formation inside the capillary.

Using this code, the dynamics of laser fields and plasma formation inside an aluminum capillary with parameters close to experimentally achievable ones have been presented. It was found that the conditions of laser pulses propagation in metallic capillaries depend substantially on the intensity of the laser pulse. Particularly, the energy losses for ultraintense (10^{19} W/cm^2) laser pulses guided in aluminum capillaries can be an order of magnitude higher than in the case of low-intensity ($\lesssim 10^{16}$ W/cm^2) laser pulses for a capillary radius of $R_0=25$ μm.

The structure of laser fields and the properties of the created plasma have been studied under the conditions of best matching (when the energy contained in the first mode reaches its maximum) and for more tight focusing of the laser pulse. It was found in the last case that longitudinal and transverse energy fluxes undergo much deeper oscillations with z than in the case of best matching. This fact is directly connected with the larger amount of energy in the second mode under conditions far from best matching. The case of best matching leads to the smallest oscillations of the laser field properties at large z but to more complex and higher frequency oscillations near the capillary entrance due to diffraction at the capillary walls. A way to reduce diffraction effects is to minimize the initial field amplitude at the capillary walls, for example by using a diaphragm to achieve a transverse profile of the laser pulse close to an Airy function, or by reducing the initial value of r_0/R_0 by using the cone-shaped capillary entrance.[8]

The model described here represents an effective tool for the investigation of intense laser fields propagation over large distances inside capillary wave guides and the determination of the characteristics of the plasma created at the capillary wall by the transverse energy flux. In particular, the information about the properties of such a plasma is of importance for experiments, planned by the Laboratoire de Physique des Gaz et des Plasmas (France) and aimed at the creation of an active medium inside metallic capillary tubes for the generation of x-ray sources.

ACKNOWLEDGMENTS

This work was supported in part by the EURATOM-C.E.A. contract V.3441.001; M.V. was supported by the French Ministère de l'Education, de la Recherche et de la Technologie and by a Young Scientist INTAS Fellowship under contract No. 03-55-1054; N.A. and M.V. were partially supported by the Russian Foundation for Basic Research, grant No. 04-02-17055.

APPENDIX: DERIVATION OF EQS. (5)–(7)

We start from Maxwell equations for the high frequency fields

$$\mathrm{rot}\,\tilde{\boldsymbol{E}}=\frac{1}{c}\frac{\partial\tilde{\boldsymbol{B}}}{\partial t},\quad \mathrm{rot}\,\tilde{\boldsymbol{B}}=\frac{1}{c}\frac{\partial\tilde{\boldsymbol{E}}}{\partial t}+\frac{4\pi}{c}\tilde{\boldsymbol{J}},\tag{A1}$$

where $\tilde{\boldsymbol{J}}$ is the plasma current.

The amplitude of the high frequency field $\tilde{\boldsymbol{E}}$ is written as $\tilde{\boldsymbol{E}}=\mathrm{Re}[\hat{\boldsymbol{E}}\exp(-i\omega_0 t)]$, where $\hat{\boldsymbol{E}}$ is the amplitude of the electric field slowly varying in time, $\hat{\boldsymbol{E}}\equiv\boldsymbol{E}\exp(ik_0 z+i\phi)$, and $\boldsymbol{E}$ is defined by Eq. (1); similar expressions are defined for the

slowly varying amplitudes of the magnetic field $\hat{\boldsymbol{B}}$ and the current $\hat{\boldsymbol{J}}$. The wave equations for the electric and magnetic fields obtained from (A1) are then

$$\nabla^2\hat{\boldsymbol{E}}+\frac{\omega_0^2}{c^2}\varepsilon\hat{\boldsymbol{E}}+\left(2i\frac{\omega_0}{c^2}\frac{\partial}{\partial t}-\frac{1}{c^2}\frac{\partial^2}{\partial t^2}\right)\hat{\boldsymbol{E}}=\nabla(\mathrm{div}\,\hat{\boldsymbol{E}}), \tag{A2}$$

$$\nabla^2\hat{\boldsymbol{B}}+\frac{\omega_0^2}{c^2}\varepsilon\hat{\boldsymbol{B}}+\left(2i\frac{\omega_0}{c^2}\frac{\partial}{\partial t}-\frac{1}{c^2}\frac{\partial^2}{\partial t^2}\right)\hat{\boldsymbol{B}}=-\left[\nabla\ln\varepsilon\times\mathrm{rot}\,\hat{\boldsymbol{B}}\right], \tag{A3}$$

where $\hat{\boldsymbol{J}}=\sigma\hat{\boldsymbol{E}}$, and the plasma permittivity $\varepsilon=1+(4\pi i/\omega_0)\sigma$ were used, and the time derivatives of the conductivity σ as well as of the field amplitudes in the terms containing σ were omitted. The z components of Eqs. (A2) and (A3) for the amplitudes slowly varying in time and space can be written, using the dimensionless variables defined by Eq. (4) and the equation $\mathrm{div}(\varepsilon\hat{\boldsymbol{E}})=0$, in the form

$$\left[\Delta_\rho+\frac{1}{\rho^2}+2i\frac{\partial}{\partial\zeta}+2\partial^2_{\zeta\xi}-\frac{\partial^2}{\partial\xi^2}+\varepsilon-1\right]\begin{Bmatrix}E_z\\B_z\end{Bmatrix}=-i\begin{Bmatrix}E_r\\B_r+\dfrac{\partial}{\partial\rho}B_z\end{Bmatrix}\frac{\partial\ln\varepsilon}{\partial\rho}, \tag{A4}$$

where the fact that ε does not depend on ϕ for circularly polarized light was taken into account and only the main radial derivatives of ε were kept.

With the same assumptions, the radial and angular components of Eq. (A1) are obtained as

$$\left(1-i\frac{\partial}{\partial\xi}\right)B_r=\frac{E_z}{\rho}-\left[1-i\left(\frac{\partial}{\partial\zeta}-\frac{\partial}{\partial\xi}\right)\right]E_\phi, \tag{A5}$$

$$\left(1-i\frac{\partial}{\partial\xi}\right)B_\phi=i\frac{\partial E_z}{\partial\rho}+\left[1-i\left(\frac{\partial}{\partial\zeta}+\frac{\partial}{\partial\xi}\right)\right]E_r, \tag{A6}$$

$$\left(\varepsilon-i\frac{\partial}{\partial\xi}\right)E_r=-\frac{B_z}{\rho}+\left[1-i\left(\frac{\partial}{\partial\zeta}+\frac{\partial}{\partial\xi}\right)\right]B_\phi, \tag{A7}$$

$$\left(\varepsilon-i\frac{\partial}{\partial\xi}\right)E_\phi=-i\frac{\partial B_z}{\partial\rho}-\left[1-i\left(\frac{\partial}{\partial\zeta}-\frac{\partial}{\partial\xi}\right)\right]B_r. \tag{A8}$$

Neglecting small time and longitudinal derivatives for the radial components of the electric and magnetic field in Eqs. (A5)–(A8) gives Eqs. (7). Neglecting higher order dispersion ($\partial^2/\partial\xi^2$ term) in Eqs. (A4) with Eqs. (7) gives Eq. (5).

To get Eqs. (6) for the angular components, only the first order derivatives in the longitudinal direction are kept; these terms are important in rarefied plasmas when $|\varepsilon-1|\ll 1$ and give rise to Eqs. (11), while in capillary wall all small derivatives in time and longitudinal direction can be neglected and result in Eqs. (14).

As can be seen from Eqs. (A5)–(A8), the small parameters that allow to make the simplifications used in this paper are the small ratios of the laser period and wavelength to the respective characteristic time and space variations of the laser envelope and produced plasma.

[1] E. Esarey, P. Sprangle, J. Krall, and A. Ting, IEEE Trans. Plasma Sci. **24**, 252 (1996), and references therein.
[2] IEEE special issue on generation of coherent radiation using plasmas, IEEE Trans. Plasma Sci. **21**, 1 (1993).
[3] H. M. Milchberg, C. G. Durfee III, and T. J. McIlrath, Phys. Rev. Lett. **75**, 2494 (1995).
[4] P. B. Corkum, N. H. Burnett, and F. Brunel, Phys. Rev. Lett. **62**, 1259 (1989).
[5] A. Y. Goltsov, D. V. Korobkin, YI. Ping, and S. Suckewer, J. Opt. Soc. Am. B **17**, 868 (2000).
[6] M. J. Adams, *An Introduction to Optical Waveguides* (Wiley, New York, 1981).
[7] D. Marcuse, *Light Transmission Optics* (Van Nostrand Reinhold, New York, 1972).
[8] Y. Kitagawa, Y. Sentoku, S. Akamatsu, W. Sakamoto, R. Kodama, K. A. Tanaka, K. Azumi, T. Norimatsu, T. Matsuoka, H. Fujita, and H. Yoshida, Phys. Rev. Lett. **92**, 205002 (2004).
[9] B. Cros, C. Courtois, G. Matthieussent, A. Di Bernardo, D. Batani, N. Andreev, and S. Kuznetsov, Phys. Rev. E **65**, 026405 (2002).
[10] N. E. Andreev, C. Courtois, B. Cros, L. M. Gorbunov, and G. Matthieussent, Phys. Rev. E **64**, 016404 (2001).
[11] N. E. Andreev, Y. Nishida, and N. Yugami, Phys. Rev. E **65**, 056407 (2002).
[12] N. E. Andreev, B. Cros, L. M. Gorbunov, G. Matthieussent, P. Mora, and R. R. Ramazashvili, Phys. Plasmas **9**, 3999 (2002).
[13] N. E. Andreev, M. E. Veysman, V. P. Efremov, and V. E. Fortov, High Temp. **41**, 594 (2003); N. E. Andreev, V. V. Kostin, and M. E. Veisman, Phys. Scr. **58**, 486 (1998).
[14] N. E. Andreev, I. L. Beigman, V. V. Kostin, M. Ef. Veisman, and A. M. Urnov, Proc. SPIE **3683**, 25 (1998).
[15] R. M. More, *Applied Atomic Collision Physics* (Academic, New York, 1982).
[16] I. T. Yakubov, Usp. Fiz. Nauk **163**, 35 (1993).
[17] N. W. Ashcroft and N. D. Mermin, *Solid State Physics* (International Thomson Edition, New York, 1976).
[18] A. Abrikosov, *Fundamentals of the Theory of Metals* (North-Holland, Amsterdam, 1988).
[19] W. Rozmus, V. T. Tikhonchuk, and R. Cauble, Phys. Plasmas **3**, 360 (1996).
[20] A. B. Langdon, Phys. Rev. Lett. **44**, 575 (1980).
[21] K. V. Khishchenko and P. R. Levashov, private communication (2005).